



# Robust noise region-based active contour model via local similarity factor for image segmentation



Sijie Niu <sup>a,b,c</sup>, Qiang Chen <sup>b,\*</sup>, Luis de Sisternes <sup>c</sup>, Zexuan Ji <sup>b</sup>, Zeming Zhou <sup>d</sup>, Daniel L. Rubin <sup>c,e</sup>

<sup>a</sup> School of Information Science and Engineering, University of Jinan, Jinan, 250022, China

<sup>b</sup> School of Computer Science and Engineering, Nanjing University of Science and Technology, Nanjing 210094, China

<sup>c</sup> Department of Radiology, Stanford University, Stanford, CA 94305, USA

<sup>d</sup> Institute of Meteorology and Oceanography, PLA University of Science and Technology, China

<sup>e</sup> Department of Medicine (Biomedical Informatics Research), Stanford University School of Medicine, Stanford, CA 94305, USA

## ARTICLE INFO

### Article history:

Received 20 September 2015

Received in revised form

11 July 2016

Accepted 12 July 2016

Available online 14 July 2016

### Keywords:

Local similarity factor

Region-based active contour

Local spatial distance

Local intensity difference

Image segmentation

## ABSTRACT

Image segmentation using a region-based active contour model could present difficulties when its noise distribution is unknown. To overcome this problem, this paper proposes a novel region-based model for the segmentation of objects or structures in images by introducing a local similarity factor, which relies on the local spatial distance within a local window and local intensity difference to improve the segmentation results. By using this local similarity factor, the proposed method can accurately extract the object boundary while guaranteeing certain noise robustness. Furthermore, the proposed algorithm completely avoids the pre-processing steps typical of region-based contour model segmentation, resulting in a higher preservation of image details. Experiments performed on synthetic images and real word images demonstrate that the proposed algorithm, as compared with the state-of-art algorithms, is more efficient and robust to higher noise level manifestations in the images.

© 2016 Elsevier Ltd. All rights reserved.

## 1. Introduction

Image segmentation plays a key role in both image understanding and computer vision. Numerous image segmentation methods have been proposed for different applications. Of special interest are those based on active contour models [1–5], which have been widely studied and used due to their ability to adaptively handle the changes of topological structure and smooth behavior. However, their methodology is normally adapted to a particular problem, and the robust and efficient application of a particular method to images of different complexity and unknown noise manifestations is still a challenging problem.

The principle of active contour model is based on the theory of contour evolution under given constraints to more accurately detect the object boundaries. As a consequence, depending on the kind of information used, existing active contour models are normally categorized into several types: edge-based models [1,3,4,6–11], global region-based models [5,12–16], edge/region-based

active contour models [17], local region-based active contour models [18–29] and global/local region-based active contour models [30]. Edge-based models design a gradient stop function to accurately segment object boundaries in high quality images, while they are more sensitive to image noise and boundaries presenting weak gradient magnitude.

Global region-based models [5,12–16] attempt to solve the above problems by using the statistical information inside and outside active contour to guide the curve evolution. Although global region-based models have several advantages over edge-based models, including less sensitivity to noise and a better ability to detect weak boundaries, these models would fail to segment images having intensity inhomogeneity. Later, local region-based models [19,21–29] were presented to overcome this problem, using localized image information as constraints. The consideration of intensity statistics in localized regions instead of globally throughout the image improves segmentation performance on images with intensity inhomogeneity, but at the expense of a higher dependency on initialization parameters.

Although both global and local region-based models improve segmentation performance assuming weak to moderate Gaussian noise, these models still lack enough robustness to be applied to wider noise manifestations observed in real world applications, especially in cases with no a priori knowledge of noise characteristics.

\* Corresponding author.

E-mail addresses: [sjniu@hotmail.com](mailto:sjniu@hotmail.com) (S. Niu), [chen2qiang@njust.edu.cn](mailto:chen2qiang@njust.edu.cn) (Q. Chen), [lsisternes@gmail.com](mailto:lsisternes@gmail.com) (L. de Sisternes), [jizexuan@njust.edu.cn](mailto:jizexuan@njust.edu.cn) (Z. Ji), [zeming\\_zhou@yahoo.com.cn](mailto:zeming_zhou@yahoo.com.cn) (Z. Zhou), [dlrubin@stanford.edu](mailto:dlrubin@stanford.edu) (D.L. Rubin).

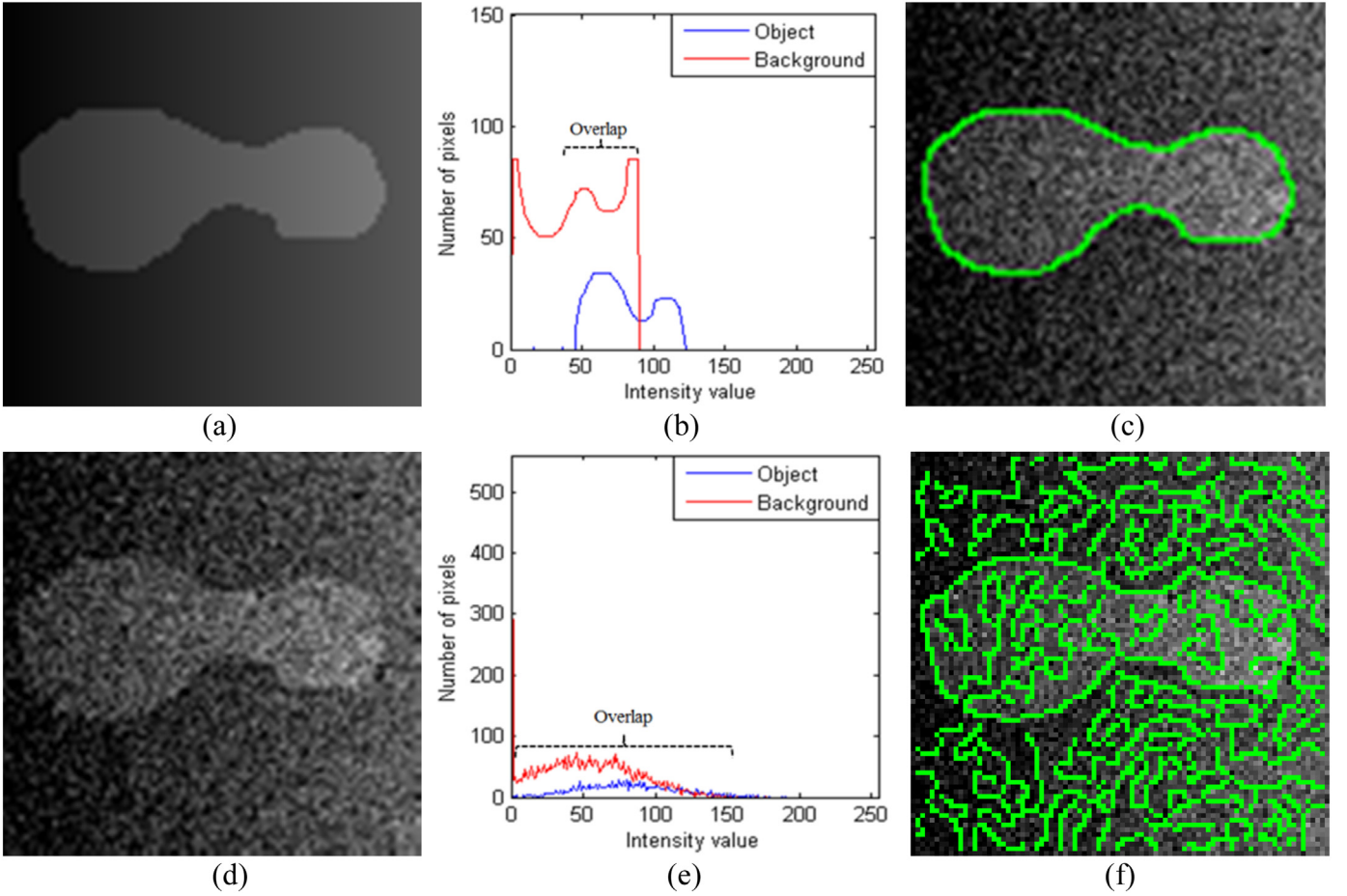


**Fig. 1.** Segmentation example in an image presenting intensity inhomogeneity corrupted by artificial noise. (a) and (d) are the inhomogeneity image and noise image, respectively, (b) and (e) indicate the intensity distribution of object and background in (a) and (d), respectively, (c) and (f) show a manually draw outline and unsuccessful segmentation results, as obtained using methods in [29].

Fig. 1 shows an example synthetic image showing intensity inhomogeneity in (a), and artificially corrupted by Gaussian noise with signal-to-noise ratio (SNR) of 4.2 dB in (d). We can observe the higher overlap in intensity values between object and background pixels after the image is corrupted by the Gaussian noise (compare Fig. 1(b)–(e)), which would make previous models [7,18,21,22,29] fail to accurately segment the object. Fig. 1(c) shows a manual outline drawn in the object to identify, while the state-of-art model [29] based on the local region has an unsuccessful segmentation result as shown in Fig. 1(f). For many types of images in real world applications, such as medical images or synthetic aperture radar (SAR) images, a successful segmentation algorithm needs to overcome wider manifestations of noise type and strength. Therefore, improving the robustness to noise of region-based active contour models is necessary.

We propose a novel region-based segmentation method that takes into account local similarity information in order to solve these limitations. The proposed method is able to segment objects from the image background with high noise levels as well as in images presenting intensity inhomogeneity. In this work we make three main contributions: first, we propose a local similarity factor to preserve noise robustness and outlier resistance, considering spatial distances and intensity differences in local regions. Second, our proposed algorithm was adapted to eliminate the necessity of pre-processing steps that frequently lead to loss of image details. Common pre-processing operations may blur object boundaries causing results that are too smooth or boundary leakage. Moreover, the proposed local similarity factor was designed to change from pixel-to-pixel and iteration-to-iteration. Therefore, the proposed method is expected to

preserve more image details. Third, we present an extensive experimental analysis of both in our method and state-of-art models on synthetic images and real images, and show that the performance of our method was best providing more accurate segmentation results while also preserving edge information.

The rest of the paper is summarized as follows. We first review the previous work in Section 2. Then we describe the methodology of our proposed approach in Section 3. The experimental results and analysis are provided in Section 4, Section 5 summarizes conclusions.

## 2. Previous work

### 2.1. C–V model

For a given image  $I(x)$  in the image domain  $x \in \Omega$  and a closed contour curve  $C$  represented by level set function  $\Phi(x)$  partitioning the image into object and background regions, the region-based model proposed by Chan and Vese [5] (C–V model) is formulated in terms of the level set function as follows:

$$\begin{aligned}
 E^{CV}(\Phi, c_1, c_2) = & \mu \int_{\Omega} \delta(\Phi(x)) |\nabla \Phi(x)| dx \\
 & + \lambda_1 \int_{\Omega} |I(x) - c_1|^2 H(\Phi(x)) dx \\
 & + \lambda_2 \int_{\Omega} |I(x) - c_2|^2 (1 - H(\Phi(x))) dx
 \end{aligned} \quad (1)$$

where  $\mu \geq 0$  is fixed constant parameter.  $\lambda_1$  and  $\lambda_2$  control the contributions of the internal energy and external energy terms, respectively, where object regions taken as internal term are the interior of  $\Phi(x)$  ( $\Phi(x) > 0$ ) and background regions considered as external term are the exterior ( $\Phi(x) < 0$ ) while ( $\Phi(x) = 0$ ) represents zeros level set.

In practice, the Heaviside function  $H$  is approximated by a smooth function  $H_\epsilon$  defined as:

$$H_\epsilon(z) = \frac{1}{2} \left[ 1 + \frac{2}{\pi} \arctan\left(\frac{z}{\epsilon}\right) \right], \quad z \in R \quad (2)$$

The derivative of  $H_\epsilon$  is  $\delta_\epsilon(z) = \frac{1}{\pi} \frac{\epsilon}{\epsilon^2 + z^2}$ .

Considering the approximated version of the functions  $H_\epsilon$  and  $\delta_\epsilon$ , the energy functional (1) is approximated as:

$$\begin{aligned} E_\epsilon^{CV}(\Phi, c_1, c_2) = & \mu \int_{\Omega} \delta_\epsilon(\Phi(x)) |\nabla \Phi(x)| dx \\ & + \lambda_1 \int_{\Omega} |I(x) - c_1|^2 H_\epsilon(\Phi(x)) dx \\ & + \lambda_2 \int_{\Omega} |I(x) - c_2|^2 (1 - H_\epsilon(\Phi(x))) dx \end{aligned} \quad (3)$$

$c_1$  and  $c_2$  are the average intensities of the image/inside and outside  $\Phi(x)$ , respectively. The average intensities  $c_1$  and  $c_2$  are calculated as:

$$c_1 = \frac{\int_{\Omega} I(x) H_\epsilon(\Phi(x)) dx}{\int_{\Omega} H_\epsilon(\Phi(x)) dx}, \quad c_2 = \frac{\int_{\Omega} I(x) (1 - H_\epsilon(\Phi(x))) dx}{\int_{\Omega} (1 - H_\epsilon(\Phi(x))) dx} \quad (4)$$

Keeping  $c_1$  and  $c_2$  fixed, we minimize the energy functional (3) with respect to  $\Phi(x)$  using the standard gradient descent method as:

$$\frac{\partial \Phi(x)}{\partial t} = \delta_\epsilon(\Phi(x)) \left[ \mu \operatorname{div} \left( \frac{\nabla \Phi(x)}{|\nabla \Phi(x)|} \right) - \lambda_1 (I(x) - c_1)^2 + \lambda_2 (I(x) - c_2)^2 \right] \quad (5)$$

Obviously, both  $c_1$  and  $c_2$  are two constants that approximate the average intensity inside and outside the active contour, respectively. However, if the intensities inside or outside the contour are not homogeneous, only using global image information might be inadequate to characterize the image content. Thus, C–V model may fail to segment images with intensity inhomogeneity.

## 2.2. LBF model

To solve the segmentation problems caused by possible image inhomogeneity, Li et al. [19] proposed the local binary fitting model (LBF) which utilized the local image information with a Gaussian kernel. The local fitting energy is defined as:

$$\begin{aligned} E^{LBF}(\Phi, f_1, f_2) = & \lambda_1 \int_{\Omega} \int_{\Omega} K_\sigma(x-y) H(\Phi(y)) |I(y) - f_1(x)|^2 dy dx \\ & + \lambda_2 \int_{\Omega} \int_{\Omega} K_\sigma(x-y) (1 - H(\Phi(y))) |I(y) - f_2(x)|^2 dy dx \\ & + \nu \int_{\Omega} |\nabla H(\Phi(x))| dx + \mu \int_{\Omega} \frac{1}{2} (|\nabla \Phi(x)| - 1)^2 dx \end{aligned} \quad (6)$$

where  $\lambda_1$ ,  $\lambda_2$ ,  $\mu$  and  $\nu$  are fixed positive parameters.  $K_\sigma$  is a Gaussian kernel function with standard deviation  $\sigma$ , and  $f_1$  and  $f_2$  indicate two varying fitting functions that approximate the local intensities on the two sides of the contour.

Using the approximated Heaviside function  $H_\epsilon$  and Dirac function  $\delta_\epsilon$ , the energy functional (6) can be rewritten as:

$$\begin{aligned} E_\epsilon^{LBF}(\Phi, f_1, f_2) = & \lambda_1 \int_{\Omega} \int_{\Omega} K_\sigma(x-y) H_\epsilon(\Phi(y)) |I(y) - f_1(x)|^2 dy dx \\ & + \lambda_2 \int_{\Omega} \int_{\Omega} K_\sigma(x-y) (1 - H_\epsilon(\Phi(y))) |I(y) - f_2(x)|^2 dy dx \\ & + \nu \int_{\Omega} |\nabla H_\epsilon(\Phi(x))| dx + \mu \int_{\Omega} \frac{1}{2} (|\nabla \Phi(x)| - 1)^2 dx \end{aligned} \quad (7)$$

Keeping the level set function fixed, and minimizing the expression in Eq. (7) with respect to  $f_1(x)$  and  $f_2(x)$ , we obtain:

$$\begin{cases} f_1(x) = \frac{K_\sigma(x) * [H_\epsilon(\Phi(x)) I(x)]}{K_\sigma(x) * H_\epsilon(\Phi(x))} \\ f_2(x) = \frac{K_\sigma(x) * [(1 - H_\epsilon(\Phi(x))) I(x)]}{K_\sigma(x) * (1 - H_\epsilon(\Phi(x)))} \end{cases} \quad (8)$$

We minimize the approximated energy functional (7) with respect to  $\Phi(x)$  to get evolving equation of the level set function:

$$\begin{aligned} \frac{\partial \Phi(x)}{\partial t} = & \mu \left( (\nabla^2 \Phi(x)) - \operatorname{div} \left( \frac{\nabla \Phi(x)}{|\nabla \Phi(x)|} \right) \right) + \nu \delta_\epsilon(\Phi(x)) \operatorname{div} \left( \frac{\nabla \Phi(x)}{|\nabla \Phi(x)|} \right) \\ & + \delta_\epsilon(\Phi(x)) (\lambda_2 e_2(x) - \lambda_1 e_1(x)) \end{aligned} \quad (9)$$

with  $e_1$  and  $e_2$  defined as follows:

$$e_i(x) = \int_{\Omega} K_\sigma(d(x, y)) |I(y) - f_i(x)|^2 dy, \quad i = 1, 2 \quad (10)$$

The LBF model handles complex images even in the presence of intensity inhomogeneity using the local intensity information in a Gaussian window inside and outside the contour. However, the LBF model is quite sensitive to noise and has limitations in the presence of high noise levels (as observed in Fig. 1).

## 2.3. Summary

Both of the C–V and LBF models employ the mean intensity inside or outside the active contour to characterize the global or local image information. Because the difference between each pixel intensity and intensity mean is statistically insufficient to characterize a region, these models may be unable to segment the images with high noise levels and intensity inhomogeneity. To address this problem, several active contour models [7] employ de-noising step to filter images, and then utilize the filtered image to define energy functional. In this work, we develop a novel region-based active contour model for the segmentations of object in images with high noise level to achieve high segmentation accuracy and good robustness by considering the local spatial information and the local intensity difference.

## 3. Proposed RLSF model

Motivated by the strengths of bilateral filtering [35] and local region-based active contour models, we proposed a robust region-based model for image segmentation called Region-based model via Local Similarity Factor (RLSF).

### 3.1. Introducing the local similarity factor

Generally, the intensity of a pixel within the image can be similar to those of its neighbors. In the RLSF model, each local region is split into two local sub-regions inside and outside the evolving curve, as shown in Fig. 2. For each pixel within a local window, the contribution of the statistical information lies on the distance from the window center. Here, the size of the local window surrounding a given position should be no larger than the size of the local region at the same position. Fig. 2 shows the relationship of the local window and local region. Black line, red circle and blue dashed rectangle represent the active contour, local region and spatial local window, respectively. Yellow region and light blue region are the local interior and exterior regions, respectively. Based on this analysis, the local spatial distance in the local similarity factor

(LSF) is included to balance the intensity difference between neighboring pixels and intensity mean on the local interior region or the local exterior region.

By introducing a local similarity factor we aim to solve two main shortcomings in existing state-of-art global and local active contour methods: (1) region-based models are less sensitive to Gaussian noise to some extent; however, they still lack enough robustness on images corrupted by noise of different characteristics and strength; (2) most methods [7] utilize the Gaussian function with a given standard deviation to filter the image, based on the assumption that the noise follows a Gaussian distribution, resulting in the boundary leakage in the curve evolution.

The local similarity factor (LSF), proposed to build the region-based energy expression is defined pixel-by-pixel within the image  $I$  by:

$$LSF(x, lc) = \int_{(y \in N_x) \neq x} \frac{\|I(y) - lc\|^2}{d(x, y)} dy \quad (11)$$

where  $N_x$  is a local window defined as a neighborhood of pixels surrounding the pixel  $x$ .  $d$  is the spatial Euclidean distance between two pixels.  $lc$  is a local average intensity value, defined within a local region as explained in a later section.

The consideration of local distances to neighbors and their local intensity differences is used to control the balance between reduction of noise effects and preservation of image details. The lack of pre-processing steps in this method aids the preservation of image details. The contribution of each pixel within a local window also depends on its proximity to the window center, which also controls the influence of noise. In our experiments, we considered the local window to be a square of  $5 \times 5$  pixel dimensions. However, local windows of other sizes or shapes, as a circle or an ellipse, could also be considered. In a later section of the manuscript we briefly explore the effects of selecting a square window of different sizes.

### 3.2. Energy functional of RLSF model

The local region-based model characterizes the background and foreground information in terms of smaller local regions. In the proposed energy functional, we define the local average intensities in the interior and exterior of the contour considering a mask  $M(x, y)$ . The mask  $M(x, y)$  is used to define a local region as:

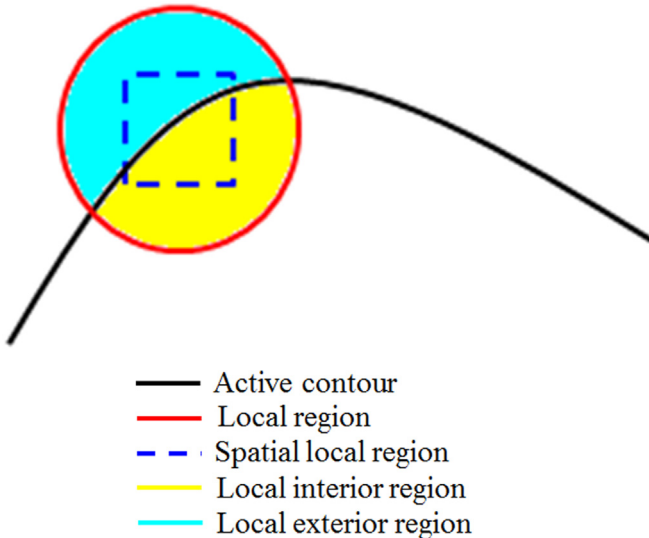


Fig. 2. The relationship of the local window and local region.

$$M(x, y) = \begin{cases} 1 & d(x, y) < r \\ 0 & \text{otherwise} \end{cases} \quad (12)$$

where  $d$  is the spatial Euclidean distance between the pixel  $y$  and the center  $x$  of a local region and  $r$  is a parameter defining the maximum size of the local region. For example, a mask corresponds to the red circle in Fig. 2. The local region defined by the parameter  $r$  and the local window defined in Eq. (11) are different, where the local region centered on the active contour is used to characterize the local intensities while the local window centered on the same position is utilized to compute the weighted values.

Based on the theory of global mean intensities of the interior and exterior regions, the localized intensity means  $lc_1$  and  $lc_2$  are then defined by:

$$lc_1(x) = \frac{\int_{\Omega} M(x, y) I(y) H_{\varepsilon}(\Phi(y)) dy}{\int_{\Omega} M(x, y) H_{\varepsilon}(\Phi(y)) dy} \quad (13)$$

$$lc_2(x) = \frac{\int_{\Omega} M(x, y) I(y) (1 - H_{\varepsilon}(\Phi(y))) dy}{\int_{\Omega} M(x, y) (1 - H_{\varepsilon}(\Phi(y))) dy} \quad (14)$$

where  $lc_1$  and  $lc_2$  represent the intensity mean in the local interior and exterior regions of active contour centered at the pixel  $x$ .  $H_{\varepsilon}(\cdot)$  is the regularized Heaviside function defined in Eq. (2).

By using the definition of local similarity factor, we now propose a robust region-based model for image segmentation, named region-based model via local similarity factor (RLSF). It incorporates local spatial distance and local intensity statistical information into its objective function, defined as:

$$E^{RLSF}(x, C) = \varepsilon^{RLSF}(lc_1(x), lc_2(x), C) + \mu \ell(C) \quad (15)$$

where  $C$  represents a closed active contour curve,  $\mu \geq 0$  is the fixed constant parameter.  $\varepsilon^{RLSF}$  and  $\ell$  are functions defined as follows:

$$\begin{aligned} \varepsilon^{RLSF}(lc_1(x), lc_2(x), C) &= \lambda_1 \int_{\text{inside}(C)} LSF(x, lc_1(x)) dx \\ &\quad + \lambda_2 \int_{\text{outside}(C)} LSF(x, lc_2(x)) dx \\ &= \lambda_1 \int_{\text{inside}(C)} \int_{(y \in N_x) \neq x} \frac{|I(y) - lc_1(x)|^2}{d(y, x)} dy dx \\ &\quad + \lambda_2 \int_{\text{outside}(C)} \int_{(y \in N_x) \neq x} \frac{|I(y) - lc_2(x)|^2}{d(y, x)} dy dx \end{aligned} \quad (16)$$

$$\ell(C) = |C| \quad (17)$$

where  $N_x$  is a local window defined as a neighborhood of pixels surrounding the pixel  $x$ , as indicated in Eq. (11).  $\text{inside}(C)$  and  $\text{outside}(C)$  are the local regions inside and outside the active contour, corresponding to the yellow region and light blue region in Fig. 2.

Using the level set solution to represent  $C$ , that is,  $C$  is the zero level set of a level set function  $\Phi(x)$ , we can write:

$$\begin{aligned} E_r^{RLSF}(x, \Phi(x)) &= \int_{\Omega} \lambda_1 \left( \int_{(y \in N_x) \neq x} \frac{|I(y) - lc_1(x)|^2}{d(y, x)} dy \right) H_{\varepsilon}(\Phi(x)) dx \\ &\quad + \int_{\Omega} \lambda_2 \left( \int_{(y \in N_x) \neq x} \frac{|I(y) - lc_2(x)|^2}{d(y, x)} dy \right) (1 - H_{\varepsilon}(\Phi(x))) dx \\ &\quad + \mu \int_{\Omega} \delta_{\varepsilon}(\Phi(x)) |\nabla \Phi(x)| dx \end{aligned} \quad (18)$$

Using the gradient descent flow method, we minimize the energy functional (18) with respect to  $\Phi$  to get the corresponding

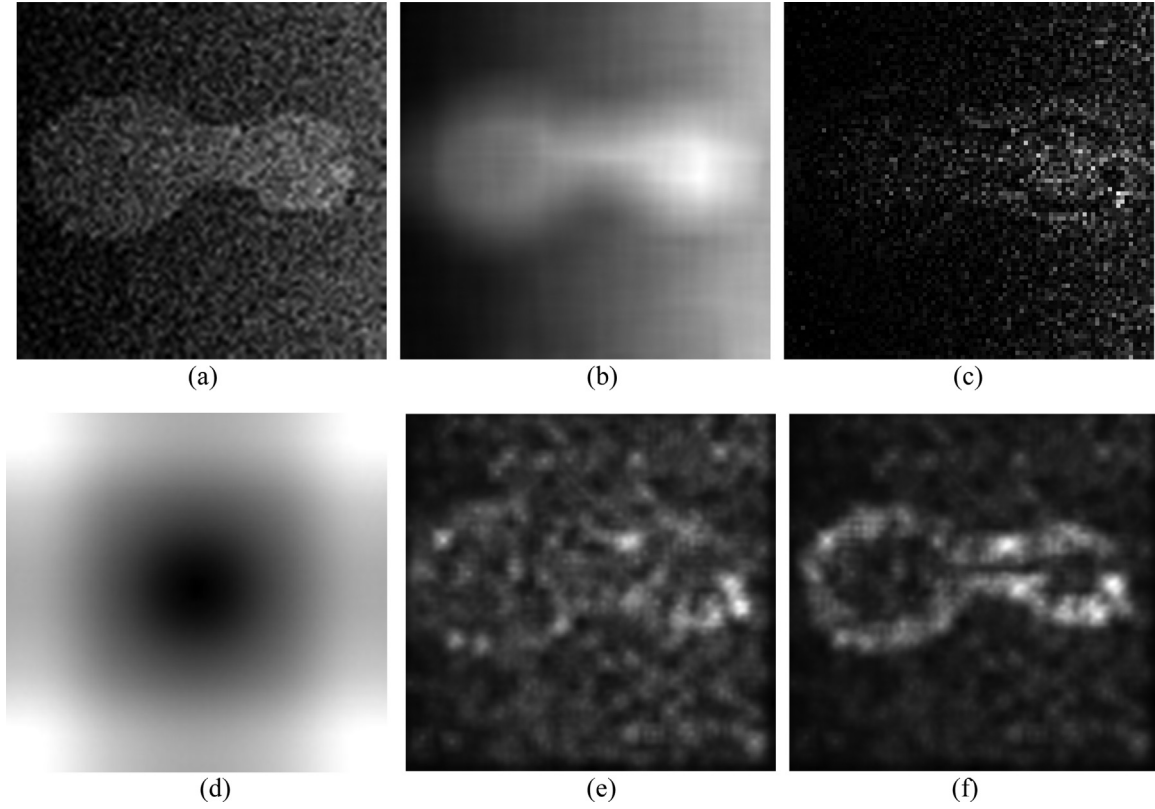


**Fig. 3.** A workflow description. (a) The original image, (b) the local average intensity  $lc_2$  defined in Eq. (19), (c) the difference image between (a) and (b), (d) the spatial distance map, (e) the  $LSF(x, lc_2(x))$  map after one iteration, (f) the  $LSF(x, lc_2(x))$  map after 700 iterations.

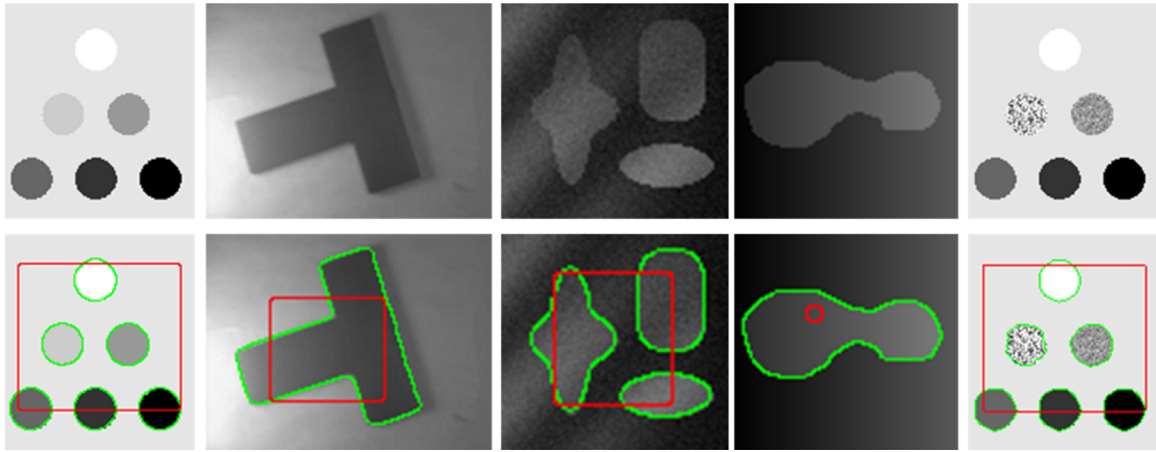


**Fig. 4.** Segmentation of synthetic images using the RLSF model. The initial contours and segmentation results are indicated in the second row with red and green outlines, respectively. (For interpretation of the references to color in this figure legend, the reader is referred to the web version of this article.)

variational level set formulation:

$$\frac{\partial \Phi(x)}{\partial t} = \delta_v(\Phi(x)) \left[ \lambda_2 \int_{(y \in N_x) \neq x} \frac{|I(y) - lc_2(x)|^2}{d(y, x)} dy - \lambda_1 \int_{(y \in N_x) \neq x} \frac{|I(y) - lc_1(x)|^2}{d(y, x)} dy \right] + \mu \delta_v(\Phi(x)) \operatorname{div} \left( \frac{\nabla \Phi(x)}{|\nabla \Phi(x)|} \right) \quad (19)$$

Note that the data term in RLSF in Eq. (19) varies from traditional C–V model [5].

An example describing the method workflow is shown in Fig. 3, where  $LSF(x, lc_2(x))$  term in Eq. (19) is displayed after one iteration in (e) and after 700 iterations in (f). The images suggest that the local similarity factor seems robust in the presence of noise,

capturing more image detail at each subsequent iteration.

### 3.3. Implementation

In the level set method [31], in order to keep the level set function  $\Phi$  as a sign distance function, the level set function is necessary to be re-initialized to be a sign distance function to its interface during the curve evolution. Consequently, we re-initialize the  $\Phi(x)$  using the incompressible two-phase flow algorithm [33]; furthermore, this algorithm also keeps the evolution curve smooth.

To obtain the solution to Eq. (19), we used the same work [21] to express it as the following iteration:

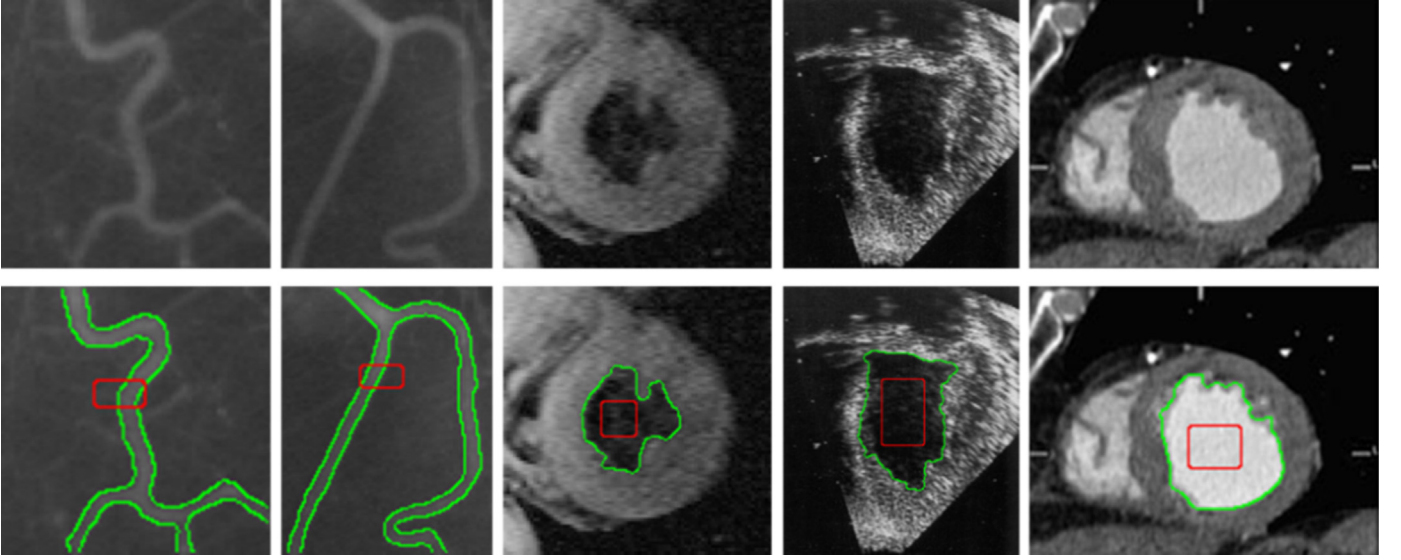


**Fig. 5.** Segmentation of five medical images using the RLSF model. First two columns: MRA images of blood vessels. Third column: MRI of the left ventricle of a human heart. Fourth column: Ultrasound image. Fifth column: Torso CT image. The original images are shown on the top row and the overlay of initial contours and segmentation results indicated in the second row with red and green outlines, respectively. (For interpretation of the references to color in this figure legend, the reader is referred to the web version of this article.)

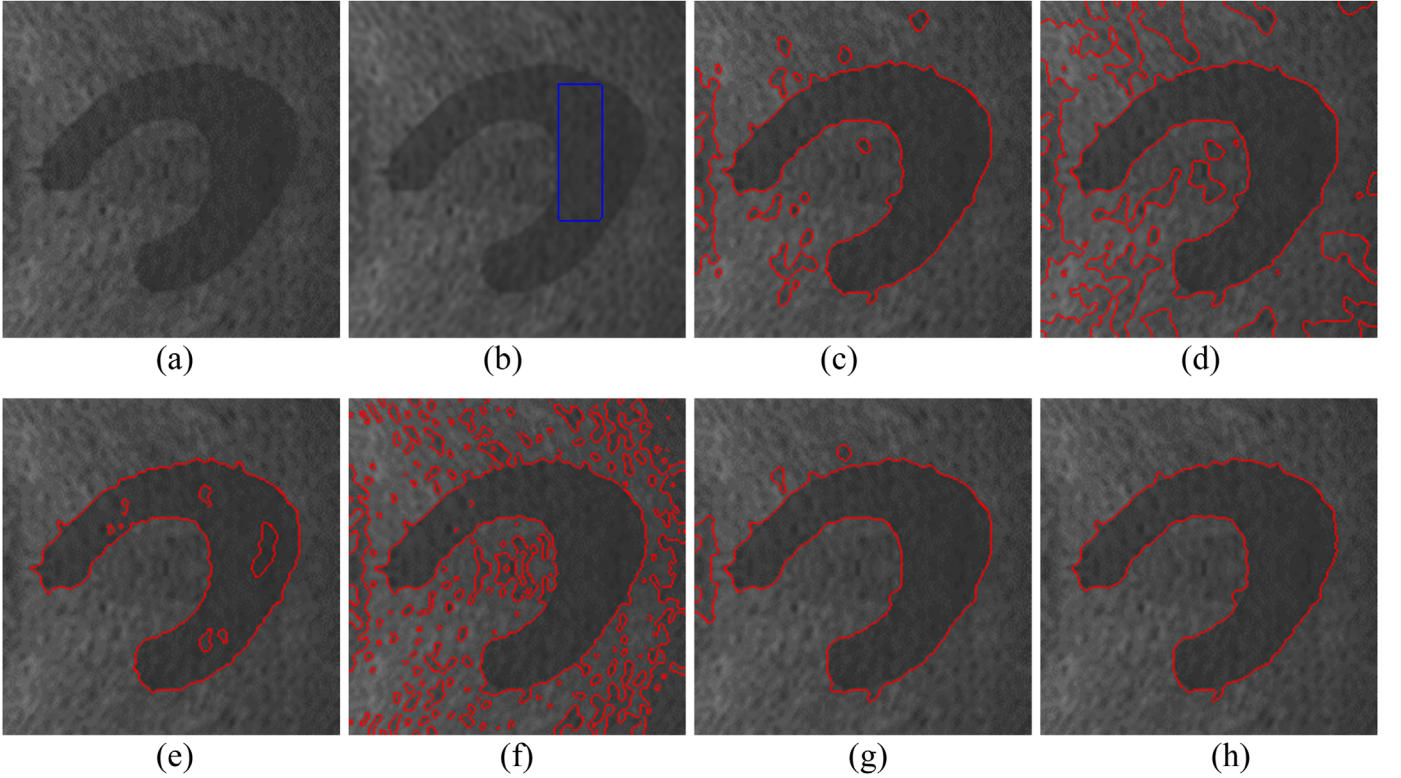


**Fig. 6.** Segmentations of the synthetic image using different models. (a) Synthetic image, (b) Initial active contour (blue outline), (c) - (h) are the segmentation results of LBF model, LIF model, LACM model, LSACM model, LLIF model, and the proposed RLSF model. (For interpretation of the references to color in this figure legend, the reader is referred to the web version of this article.)

$$\phi^{n+1}(x) = \phi^n(x) + \Delta t \Delta \phi^n(x) \quad (20)$$

where  $\Delta \phi^n(x)$  is the approximation of the right hand side in Eq. (19).  $\Delta t$  is the time-step, defined as  $\Delta t = \frac{0.48}{\max(\text{abs}(\phi^n))}$ . The solution we obtain from Eq. (20) is re-initialized to be a sign distance function and keep the level set smooth.

#### 4. Experimental results

The experiments presented in this section were all performed on a 2.16 GHz Pentium Dual PC with 3 GB memory. The algorithm was implemented in Matlab (The MathWorks, Inc.).

##### 4.1. Qualitative evaluation

We evaluated qualitatively the RLSF model results on five images of different noise type and complexity level. Fig. 4 displays

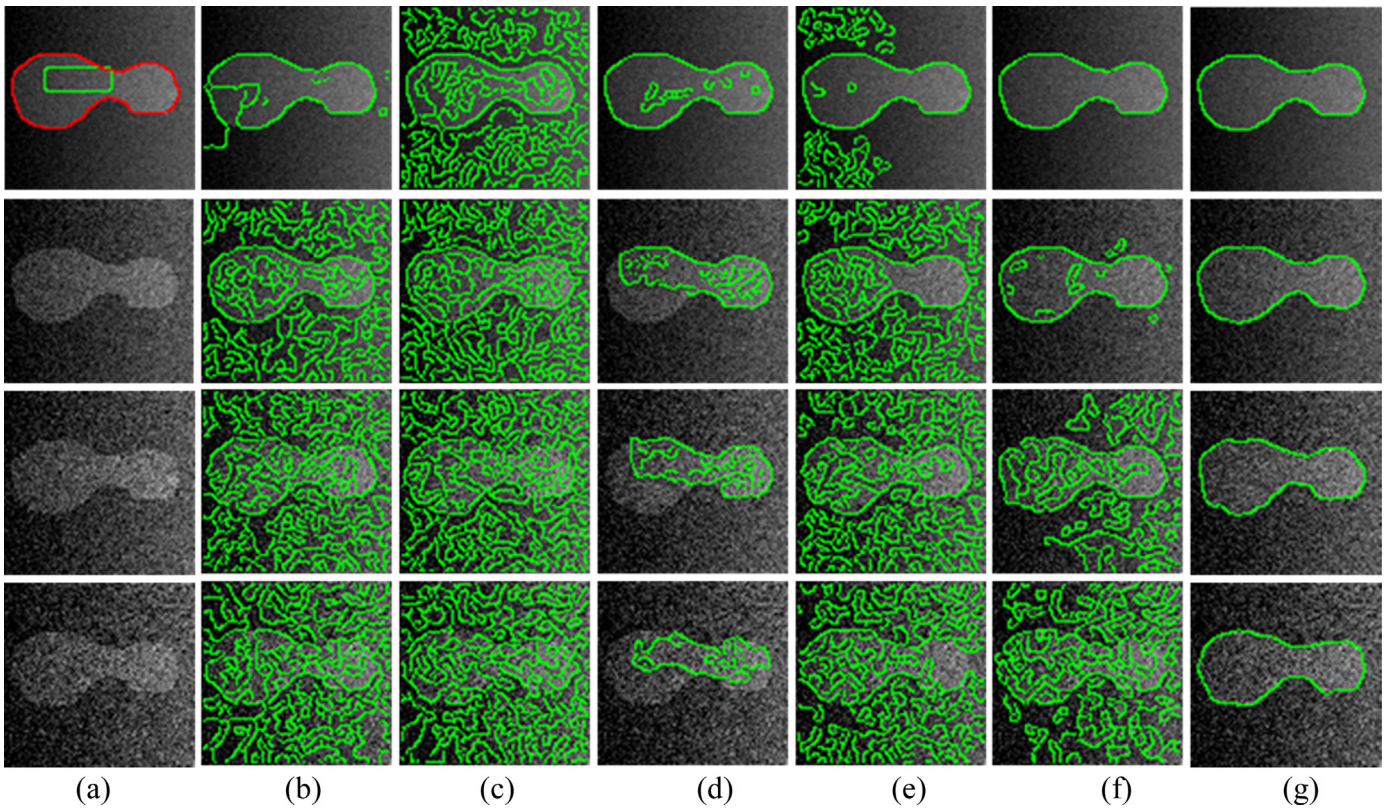


**Fig. 7.** The comparison with seven region-based active contour models on a noise image. (a) the noise image under four noise levels corresponding to first, second, third and fourth row, i.e.  $\text{SNR} = \{8.9 \text{ dB}, 5.1 \text{ dB}, 4.2 \text{ dB}, 3.9 \text{ dB}\}$ , (b)–(g) are results of LBF, LIF, LACM, LSACM, LLIF and RLSF. The initial contour (green) and ground truth (red) are overlapped to the first image in the first row. (For interpretation of the references to color in this figure legend, the reader is referred to the web version of this article.)

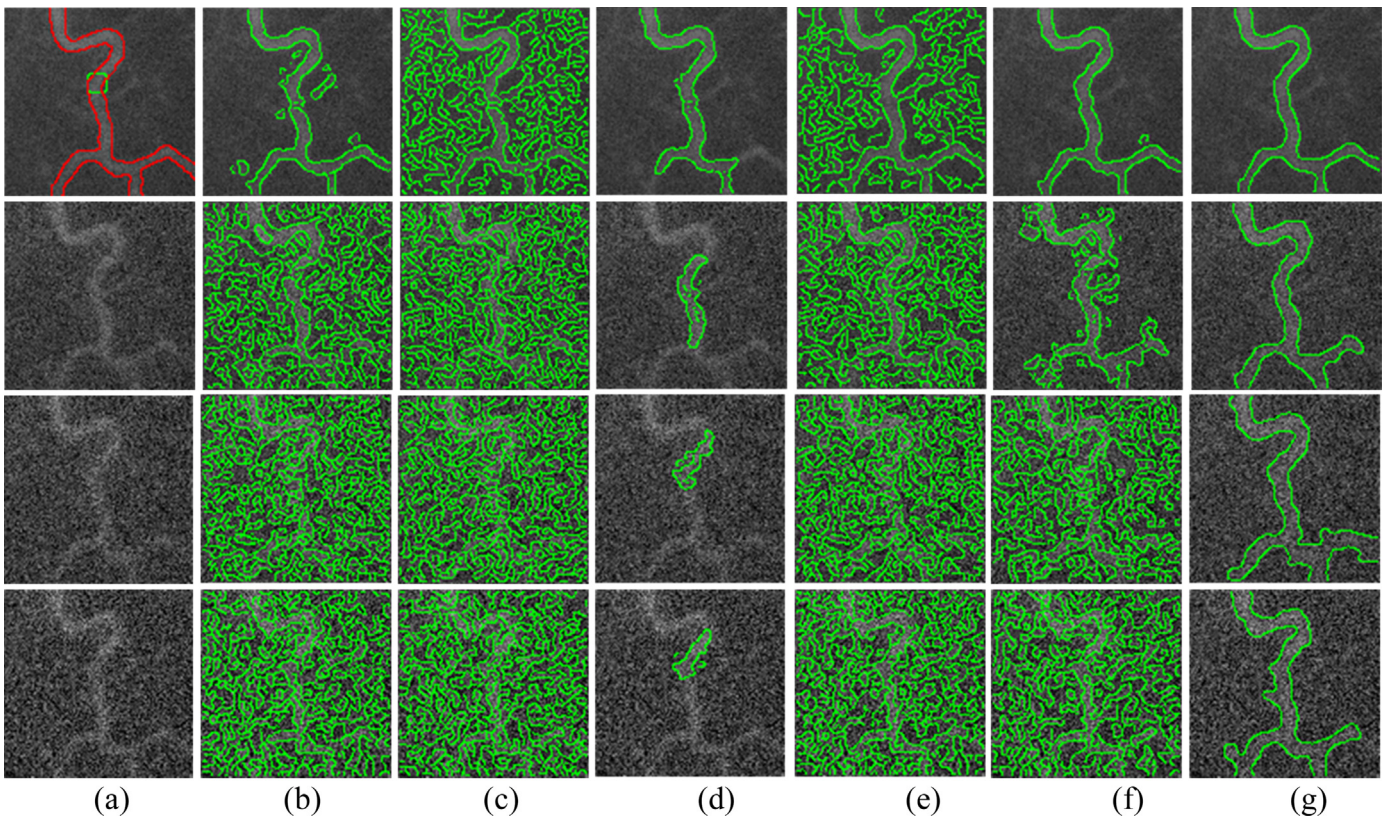


**Fig. 8.** The comparison with five region-based active contour models on a blood vessel image corrupted by Gaussian noise. (a) the noise image under four noise levels corresponding first row to fourth row, i.e.  $\text{SNR} = \{9.4 \text{ dB}, 5.5 \text{ dB}, 4.7 \text{ dB}, 4.4 \text{ dB}\}$ , (b)–(g) are the results of LBF, LIF, LACM, LSACM, LLIF and RLSF, respectively. The initial contour (green) and ground truth (red) are overlapped to the first image in the first row. (For interpretation of the references to color in this figure legend, the reader is referred to the web version of this article.)

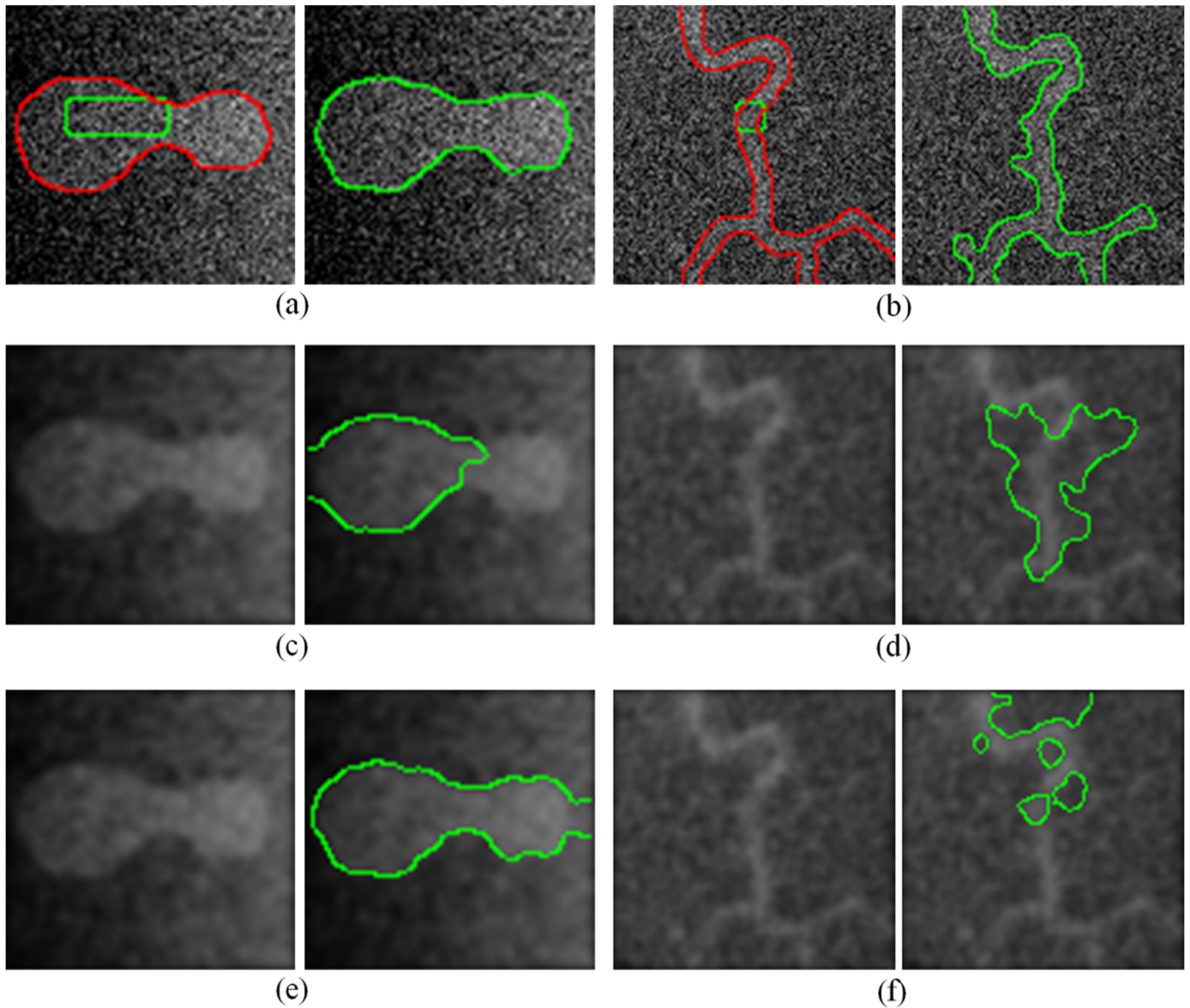


**Fig. 9.** (a) and (b) images with noise level 3.9 dB and 4.4 dB, respectively (in left), and the result of RLSF model (in right), (c) and (d) the filtered image (in left) and the result of CL model [7] (in right), (e) and (f) the filtered image (in left) and the result of LLIF model (in right). The initial contour and ground truth are shown in the images displayed in the far left in green and red, respectively. (For interpretation of the references to color in this figure legend, the reader is referred to the web version of this article.)

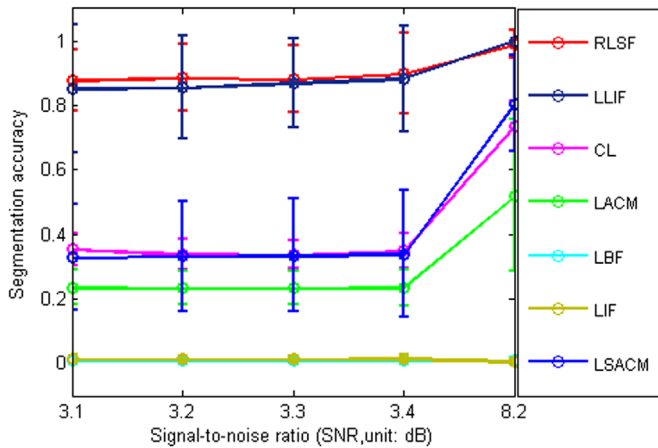


**Fig. 10.** Quantitatively comparisons of segmentation accuracy (Jaccard index) on a verification letter image dataset.

five synthetic images with severe intensity inhomogeneity. The initial contours and final segmentation results are highlighted in red and green, respectively, and overlaid on the images in the second row. We can observe that the RLSF method can segment multiple objects successfully in images with severe intensity inhomogeneity. Parameters were set to be  $\lambda_1 = \lambda_2 = 1$ ,  $\mu = 0.06$ ,  $\epsilon = 0.01$ ,  $r = 7$ . The local window considered in the local similarity factor was set to a square of  $5 \times 5$  pixel dimensions.

We also evaluated the RLSF model on a set of medical images from four different modalities. Fig. 5, from left to right, shows two magnetic resonance angiogram (MRA) images of blood vessels, a magnetic resonance image (MRI) of the left ventricle of a human heart, an ultrasound image and a torso computed tomography (CT) image. These images present high complexity levels, including different noise statistics with varying strength, low contrast and intensity homogeneity. The experiment results reveal that the RLSF model was able to accurately locate the real boundaries of all targeted objects. Parameters were set to be  $\lambda_1 = \lambda_2 = 1$ ,  $\mu = 0.06$ ,  $\epsilon = 0.01$ ,  $r = 7$ . The local window considered in the local similarity

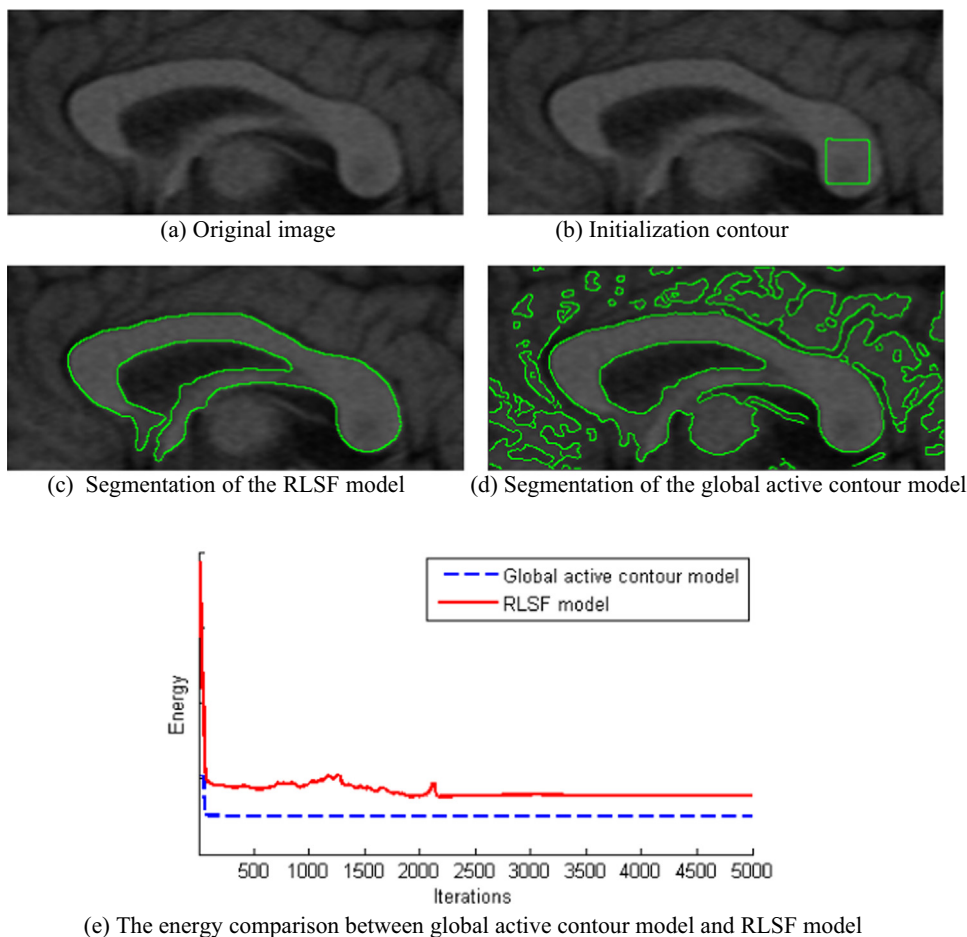


**Fig. 11.** Preliminary convergence analysis. All parameters were set to  $\lambda_1 = \lambda_2 = 1$ ,  $\mu = 0.06$ ,  $\varepsilon = 0.01$ ,  $r = 10$ ,  $d = 7$  (a) Original image, (b) Initialization contour, (c) Segmentation of the RLSF model (d) Segmentation of the global active contour model, (e) The energy comparison between global active contour model and RLSF model.

factor was set to a square of  $5 \times 5$  pixel dimensions.

To demonstrate the performance of the proposed RLSF model, we compared it with state-of-art active contour models, including local binary fitting model (LBF) [18], local image fitting model (LIF) [21], localized active contour model (LACM) [22], locally statistical active contour model (LSACM) [29] and local likelihood image fitting energy model (LLIF) [32] on a synthetic image having noise and inhomogeneous intensities. In our method, the parameters are set to  $\lambda_1 = \lambda_2 = 1$ ,  $\mu = 0.06$ ,  $\varepsilon = 0.01$ ,  $r = 15$ , and the size of local window is  $5 \times 5$ . To make a fair comparison, we used the same initial contour, and set model parameters to their default values. The synthetic image and the initial contour highlighted in blue are displayed in Fig. 6(a) and (b), respectively. The segmentation results generated by using different models are shown in Fig. 6(c)–(h), respectively. The comparison results reveal that due to modeling the inhomogeneous regions as Gaussian distribution, the LIF model and the LSACM model detect more false objects whose intensities are similar to object intensities. The LBF model, LACM model, and LLIF can detect the object boundaries, but still is affected by the background. The major difference with these models is that the proposed RLSF characterizes the local intensities along evolving curve, and then balances the local intensity differences by considering the local spatial distance. The proposed RLSF model can produce satisfactory segmentation. This experiment demonstrates that our model has an improved ability to overcome the impact of different noise level and intensity inhomogeneity.

#### 4.2. Evaluation of noise robustness

We evaluated the performance of the RLSF model in different noise levels on the synthetic and real images, comparing its results with both classical and state-of-art active contour models, including LBF, LIF, LACM, LSACM, and LLIF. To make a fair comparison, the same initial active contour curve was set for all the experiments, while the remaining method-dependent parameters were set to their default value. Artificial noise of different levels was added to the images using the *Matlab* function *imnoise*. Fig. 7 displays the comparison results obtained by using different segmentation methods on an artificial image with strong inhomogeneous intensity (corresponding to Fig. 1(a)) corrupted by Gaussian noise with SNR {8.9 dB, 5.1 dB, 4.2 dB, 3.9 dB} corresponding to the first, second, third and fourth row, respectively. Comparing to the ground truth shown in the first column, we can observe how the segmentation results produced by the LBF, LIF, LACM, LLIF and LSACM models are very sensitive to noise, as visibly worse results are produced at higher noise levels, while the RLSF model is able to accurately extract the target at all noise levels. The comparison results demonstrate that the RLSF model drives the active contour to converge to the boundary of target in the noise image while remaining more insensitive to higher noise levels.

We also evaluated the RLSF model on a blood vessel MRA image artificially corrupted by Gaussian noise at different levels, with SNR {9.4 dB, 5.5 dB, 4.7 dB, 4.4 dB} as shown in the first, second,

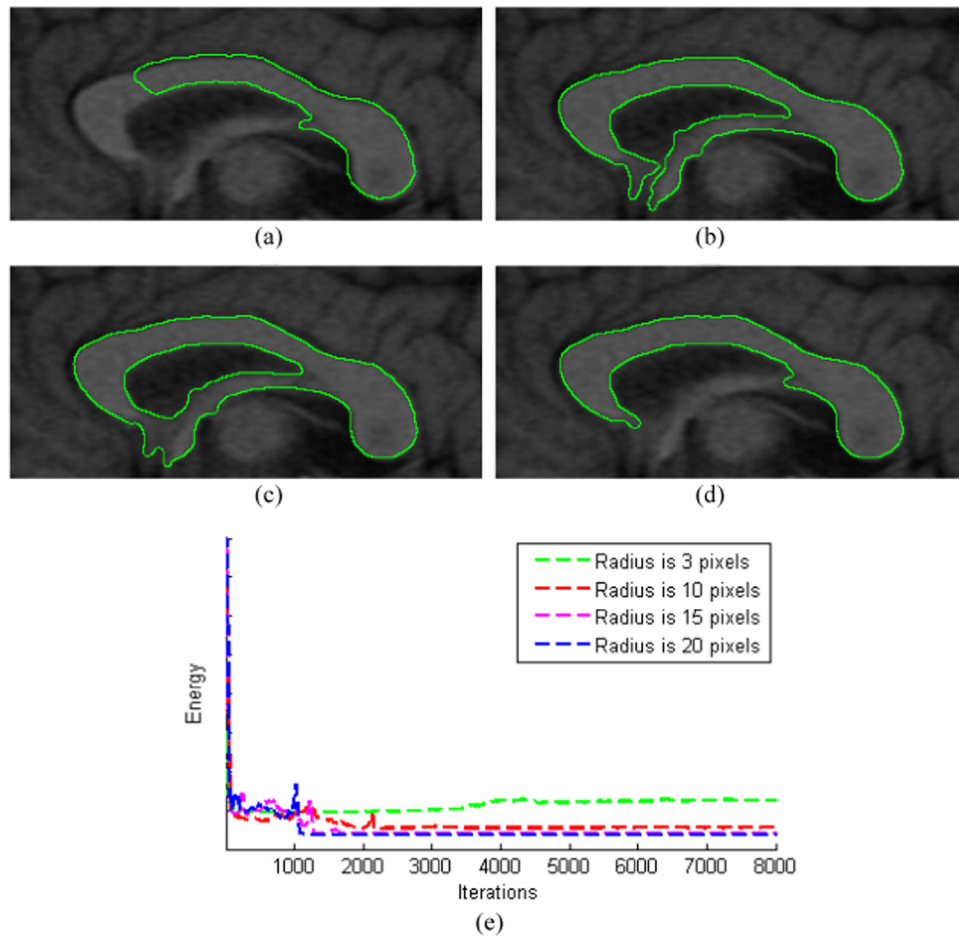


**Fig. 12.** (a)–(d) Segmentation results produced by the RLSF model using a radius size 3, 10, 15, 20 pixels, respectively. (e) The energy component recorded at each iteration. Remaining parameters were set to  $\lambda_1 = \lambda_2 = 1$ ,  $\mu = 0.06$ ,  $\varepsilon = 0.01$ ,  $d = 7$ .

third, and fourth row in Fig. 8(a), respectively. We can observe how the identification of blood vessels in the image becomes harder with increasing noise level, resulting in more difficult segmentation problem. The red contour in the first column indicates a ground truth obtained by manual segmentation on the noiseless image (the same as shown in the first column in Fig. 5). We can observe how the LBF, LIF, LACM, LLIF, and LSACM models are very sensitive to noise, especially LBF, LIF and LSACM model, while LACM model is unable to evolve the active contour toward the target boundary since the noise makes the image more complex. Our proposed RLSF model has an improved ability to overcome the impact of low contrast and noise on this image. While noise level also has an effect in the RLSF model, we can observe how the segmentation results at higher levels are still reliable, especially by comparison to the results produced by other methods. Parameters were set to be  $\lambda_1 = \lambda_2 = 1$ ,  $\mu = 0.06$ ,  $\varepsilon = 0.01$ ,  $r = 7$ . The local window considered in the local similarity factor was set to a square of  $5 \times 5$  pixel.

As shown in Figs. 7 and 8, the previous local models increased their performance when the image is corrupted by noise of lower strength, and they tended to show poor segmentation results on images with higher noise levels or with no prior knowledge about the nature of the noise. However, the RLSF model showed accurate results at the higher noise levels.

One common approach to eliminate the noise dependency of previous methods is to consider a de-noising pre-processing step. However, this process may result in loss of details or erroneous results. The RLSF method produced accurate results without any

pre-processing steps. In order to illustrate this fact, Fig. 9(a) and (d) shows the RLSF results at the highest noise levels in Figs. 7 and 8, respectively. As the Chunming Li model (CL model) [7] and the LLIF model failed to accurately segment these images, we computed their results again, but this time using a pre-processing denoising step by Gaussian filtering (1.5 pixels standard deviation and  $15 \times 15$  pixels window size), shown in Fig. 9(b) and (e) for the CL model, and (c) and (f) for the LLIF model. We can observe that although the pre-processing denoising step somehow improved the segmentation produced by these previous models, the results are still not accurate, while this procedure also blurred the boundary causing possible loss of image details. On the other hand, the RLSF method was able to directly segment the objects from images with high levels of noise without the need of the pre-processing denoising step.

We further assessed the performance of the RLSF model in the presence of different noise levels and compared to the previously mentioned methods quantitatively, segmenting a dataset of 22 verification letter images [24], where these images are corrupted by synthetic noise and serve image inhomogeneity and the ground truth is known. All the images collected were artificially corrupted by Gaussian noise at five different, with SNR {8.2 dB, 3.4 dB, 3.3 dB, 3.2 dB, 3.1 dB} in the same manner as done previously. We computed the Jaccard similarity coefficient (ratio between the intersection and union of the segmentation results and ground truth) as a quantitative measurement of segmentation accuracy and compared the results for different methods and noise levels, averaging across the images in the dataset. Fig. 10 shows the

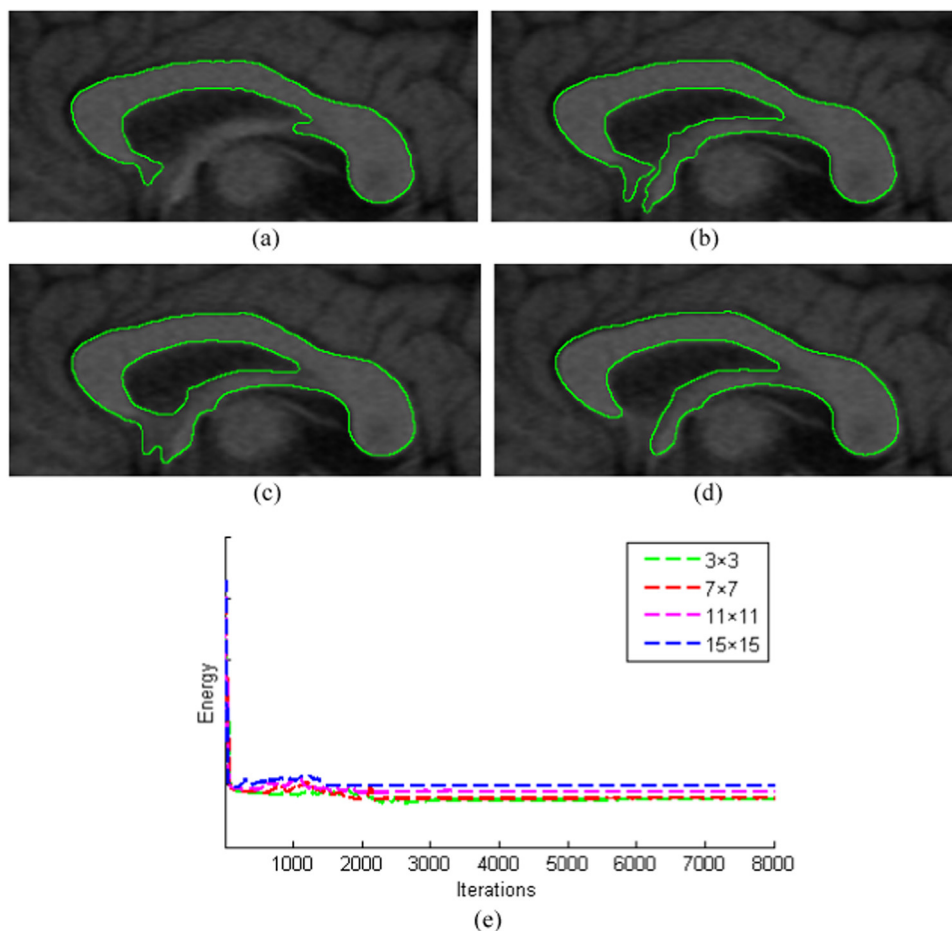


**Fig. 13.** (a)–(d) Segmentation results produced by the RLSF model using a window size  $3 \times 3$ ,  $7 \times 7$ ,  $11 \times 11$  and  $15 \times 15$ , respectively. (e) The energy component recorded at each iteration. Remaining parameters were set to  $\lambda_1 = \lambda_2 = 1$ ,  $\mu = 0.06$ ,  $\varepsilon = 0.01$ ,  $r = 10$ .

comparison result of the different models evaluated, including CL, LACM, LBF, LIF, LSACM, LLIF and RLSF models. The comparative results demonstrate that the RLSF was able to perform appropriately for the images in the dataset, even at higher levels of noise. Parameters were set to be  $\lambda_1 = \lambda_2 = 1$ ,  $\mu = 0.06$ ,  $\varepsilon = 0.01$ ,  $r = 7$ . The local window considered in the local similarity factor was set to a square of  $5 \times 5$  pixel dimensions.

#### 4.3. Discussion of convergence

We present a preliminary convergence analysis here by comparing the local and global energy variants on a brain magnetic resonance imaging (MRI), shown in Fig. 11. Fig. 11 shows in (a) the original MRI image, (b) initialization contour, (c) and (d) segmentation of the RLSF model and global active contour model, respectively, (e) the local and global energies. In this particular image, the energies converged to different values for the RLSF and the global model, producing different final segmentation results (shown in (c) and (d), respectively), and the energies shown in (e) are scaled to show them on the same graph. In Fig. 11 (e), we can observe that the RLSF model converged to a minimum energy value after  $\sim 3000$  iterations, whilst the global model converged to a stable solution after  $\sim 100$  iterations presenting a higher convergence speed. However, the faster convergence speed of the global model came with a tradeoff of worse segmentation results when compared to the RLSF model.

We also evaluated the effects of two parameters (radius and window size) on the RLSF resulting energy, results and convergence

speed. Fig. 12 shows the results of varying the radius while maintaining a constant window size. Fig. 13 shows the results of varying the window size while maintaining a constant radius. We can observe that convergence speed varies as we vary such parameters, with the energies eventually converging to a stable status. In broad terms, selecting smaller radius and window sizes needed a slightly larger number of iterations to converge. The final results followed boundaries that can be observed in the image, but depended highly on the selection these parameters. This fact highlights the need of an appropriate parameter selection dependent of the nature of the object to be segmented.

#### 4.4. Initialization robustness

One of the possible limitations of the RLSF model is its dependence on contour initialization, similar to other local active contour models, like Refs. [18,21,29,32] (which are known to be more sensitive to initialization than global active contour models). Since the RLSF model calculates the local average intensity inside and outside the active contour, the initial contour needs to be placed on a region that is relatively close to object to be segmented. The results demonstrated a successful segmentation when the initialization contour is relatively good, including a larger number of pixels belonging to the object region than belonging to the background region. Fig. 14 shows results in a larger array of initial contours on a synthetic image including three different objects with inhomogeneity. The results in four of the nine different initialization, shown in (a)–(d), were accurate and stable for

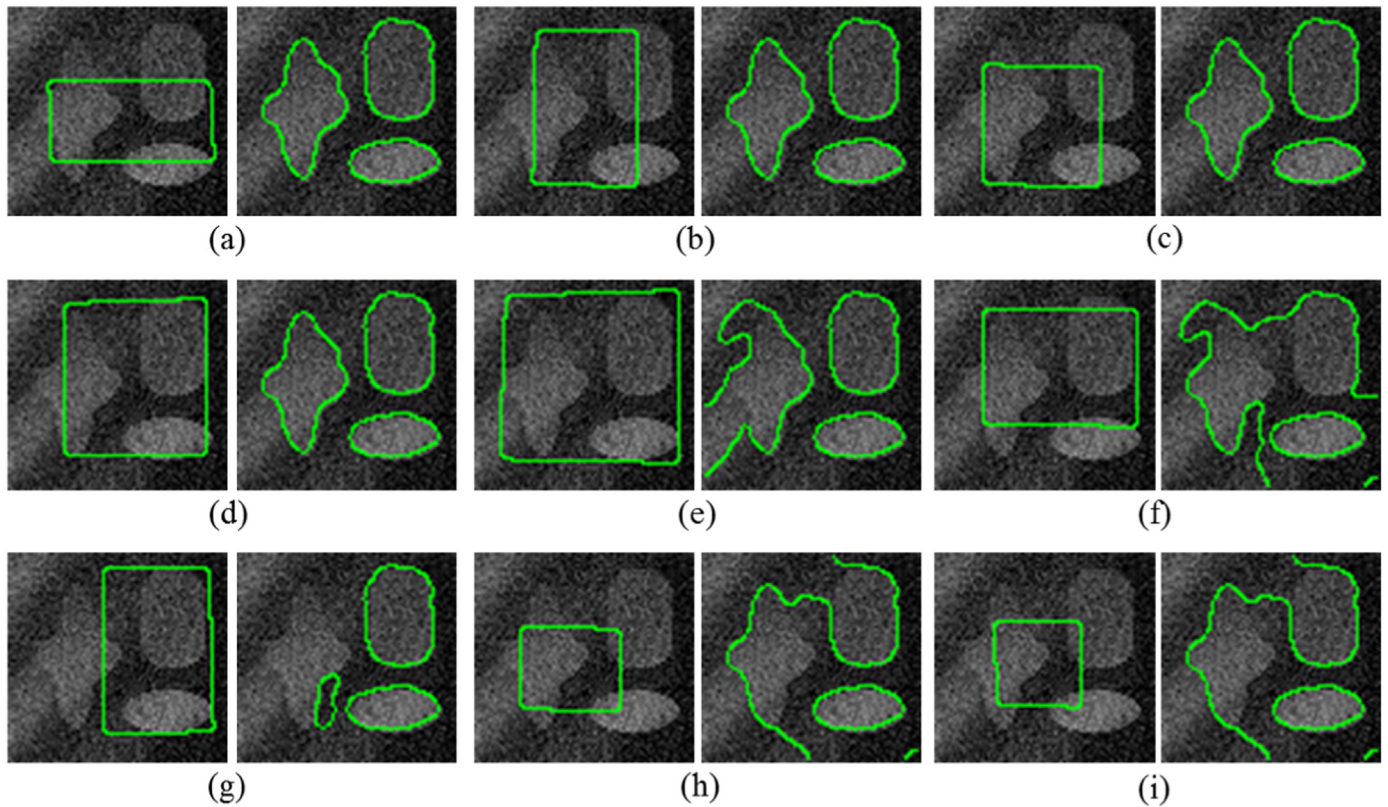


**Fig. 14.** Initialization robustness analysis of RLSF model. (a)–(i) show initialization contours in the left side and final segmentation results in the right side, respectively. The segmentations revealed that the RLSF model is able to produce robust results to certain variance in initialization; however it is affected by the initialization in cases containing too much background information relative to the object information. In these experiments, all parameters were set to  $\lambda_1 = \lambda_2 = 1$ ,  $\mu = 0.06$ ,  $\varepsilon = 0.01$ ,  $r = 10$ ,  $d = 7$ .

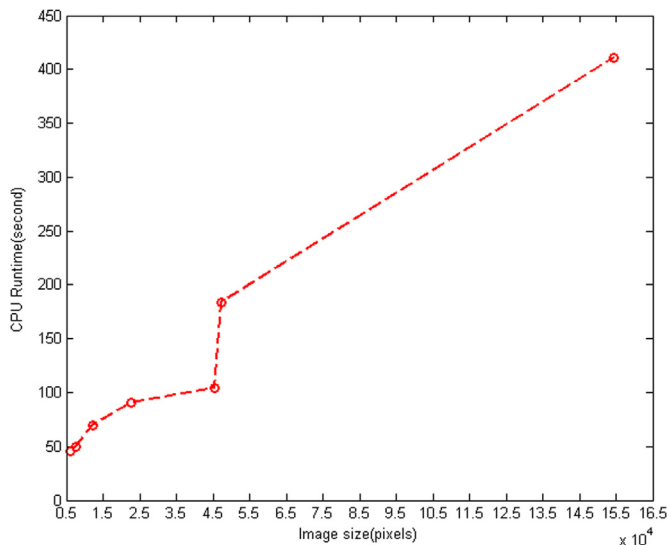


**Fig. 15.** The computational cost of the RLSF model for increasing image sizes. All parameters were set to  $\lambda_1 = \lambda_2 = 1$ ,  $\mu = 0.06$ ,  $\varepsilon = 0.01$ ,  $r = 10$ ,  $d = 7$ .

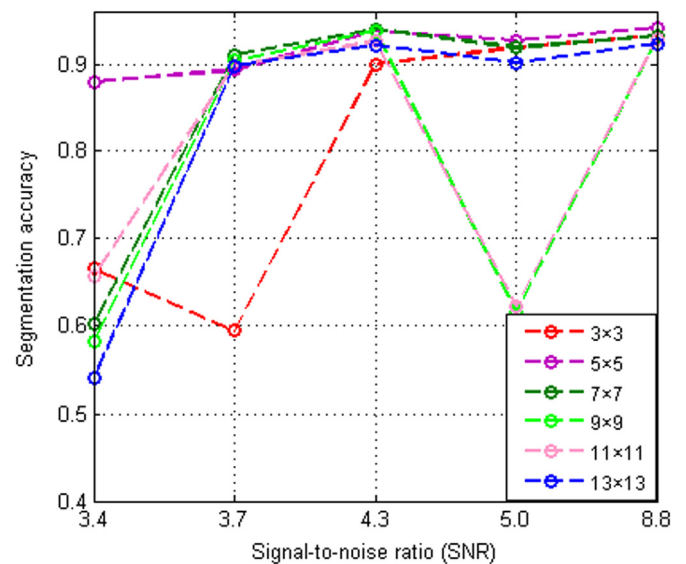


**Fig. 16.** The evaluation of the local window size.

the three objects in the image. Two initializations, shown in (e) and (g), resulted in accurate and stable segmentation of two of the objects while it failed to segment one object. The remaining 3 initializations, shown in (f), (h) and (i), resulted in an incorrect segmentation of the background region. These results highlight two limitations in selecting an initial boundary. The first limitation comes when the initialization contour contains a large amount of background information, which may result in an erroneous

segmentation of background due to inhomogeneity in the image as seen in (e). The second limitation comes when the initially selected pixels contain very reduced information about an object and more information about the background, as seen in (f)–(i), which produces the exclusion of the object and inclusion of background.

Although the RLSF model is sensitive to initialization, Fig. 14 indicates that different reasonable initializations containing enough

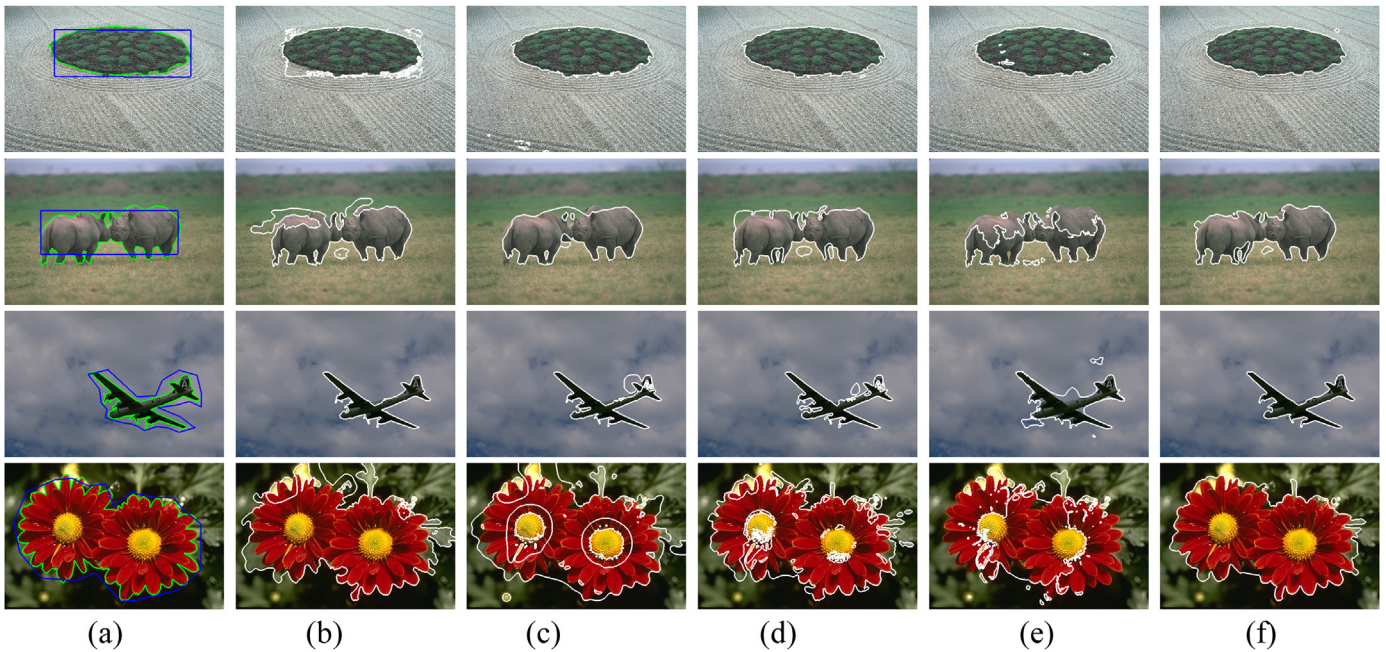


**Fig. 17.** The comparison results on the nature images. (a) the original image with manual segmentation (green) and initialization result (blue), (b)–(f) are the results of LACM, LBF, LIF, LSACM and RLSF model, respectively, with segmentation outlines indicated in white. These four images correspond to image ID 86016, 112056, 3096 and 124084, respectively. (For interpretation of the references to color in this figure legend, the reader is referred to the web version of this article.)

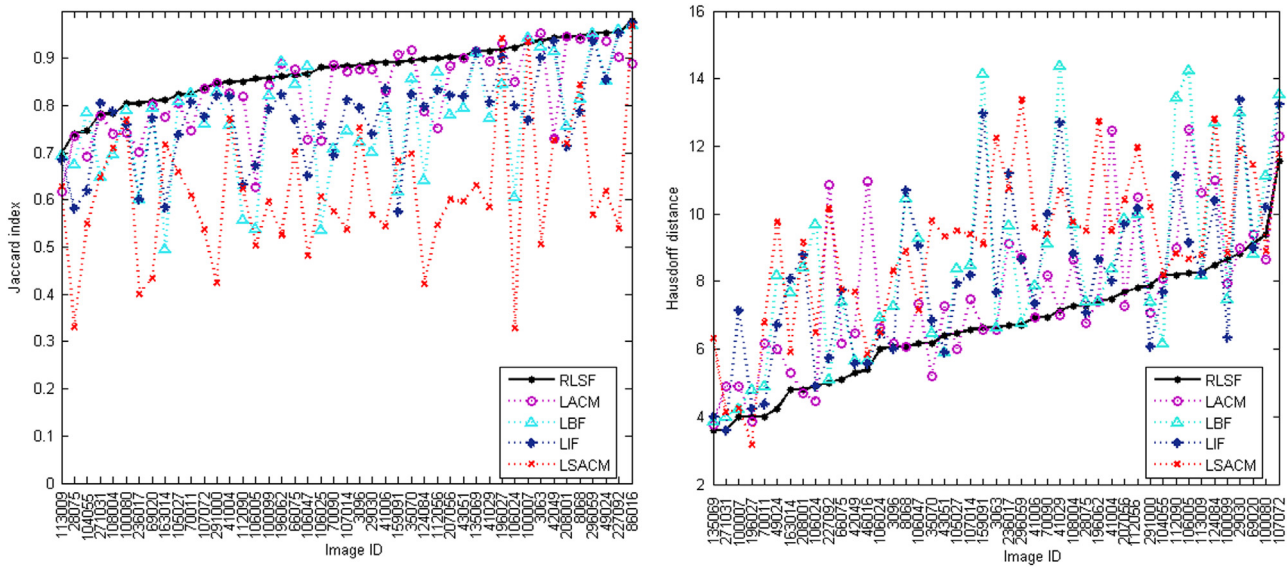


**Fig. 18.** Jaccard index and Hausdorff distance of segmentation results on 45 Berkeley color images. (For interpretation of the references to color in this figure legend, the reader is referred to the web version of this article.)

information about the objects and reduced background information produce accurate exact results. In upcoming work we also plan to include further modifications and constraints to reduce the dependency with initialization even more as well as improve the model ability to handle more complex images.

4.5. Runtime

Theoretically, the proposed RLSF model has a linear complexity  $O\left(\frac{S}{dr}\right)$ , where  $S$ ,  $d$  and  $r$  are the size of the image, window size and

radius, respectively, as shown in Fig. 15 shows the runtime performance on images of increasing sizes. Figs. 11 and 12(e) also revealed that the convergence speed will slightly decrease as the radius or window size decreased.

4.6. Local window size evaluation

The introduced RLSF model is governed by one main parameter controlling the contribution of the local similarity factor: the local window size, which specifies the set of neighborhood pixels. The parameter mainly controls the extent of noise preservation. The

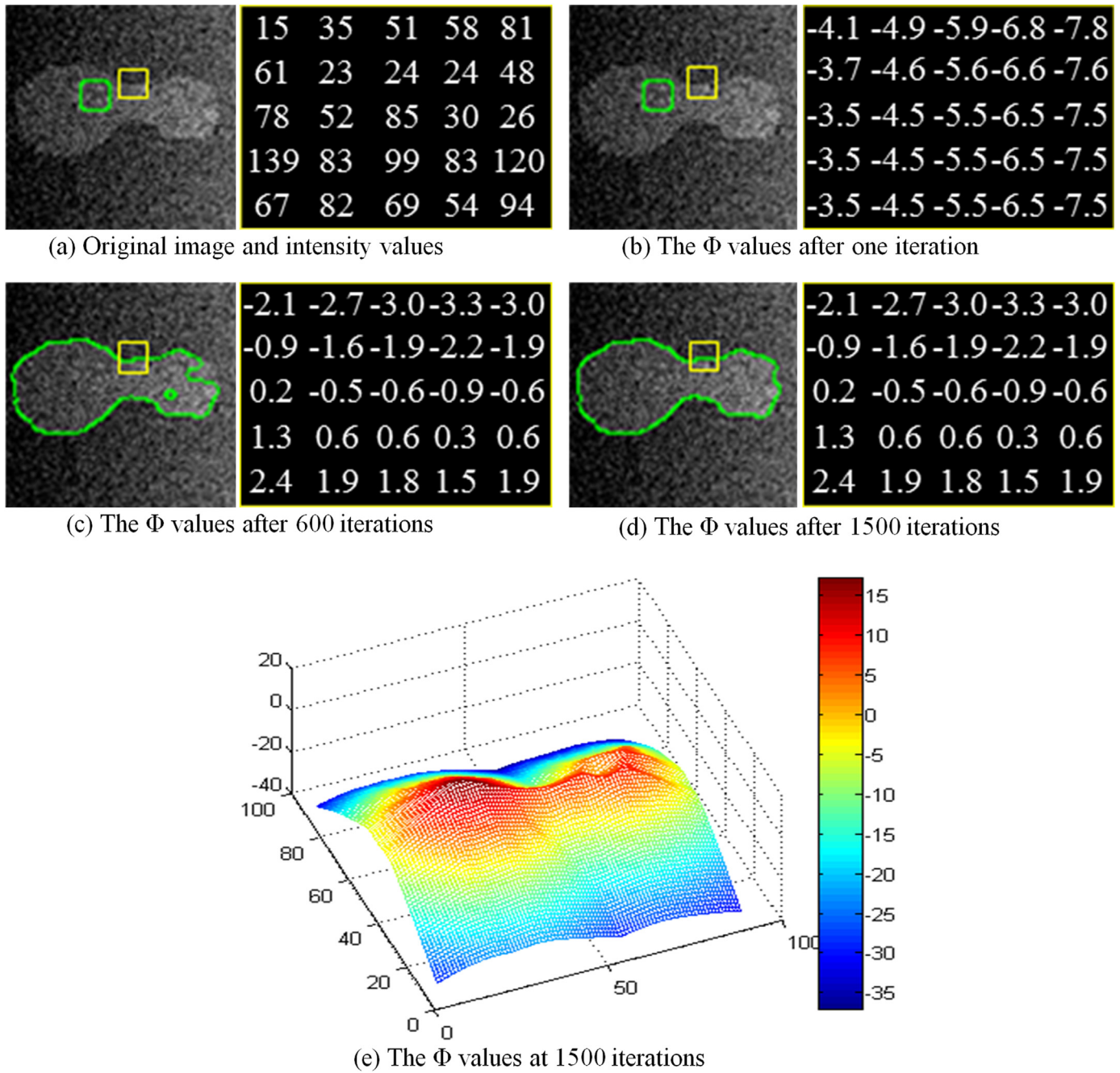


**Fig. 19.** Example displaying the contents of a  $5 \times 5$  local window with their corresponding level set function  $\Phi$  values at increasing iterations (window location indicated with a yellow outline in the images). The green rectangle indicates the evolution result at each iteration (initial contour in the first image at the top left). (e) level set function  $\Phi$  values at 1500 iterations throughout the image. (For interpretation of the references to color in this figure legend, the reader is referred to the web version of this article.)

synthetic image artificially corrupted by five Gaussian noise levels corresponding to SNR {8.8 dB, 5.0 dB, 4.3 dB, 3.7 dB, 3.4 dB} shown in Fig. 1(d) was used to study the influence of these parameter. We tested the method performance in a varying set of local window size, from  $3 \times 3$  pixels to  $13 \times 13$  pixels in increment steps of 2 pixels, with the segmentation accuracy in terms of Jaccard similarity coefficient shown in Fig. 16. We can observe that the segmentation accuracy with different local window size decreased as SNR decreased. However, the Jaccard similarity coefficient keeps relatively stable for  $5 \times 5$  pixels, where it showed the higher accuracy for this particular image.

#### 4.7. Comparison in nature image segmentation

A comparative experiment was performed on 45 real world color images selected from the Berkeley segmentation data set 500 (BDS500) which consists of a set of natural images and their ground truth segmentation maps [34], where these 45 test images (non-texture images) have only one target and relatively simple background and their sizes are all  $481 \times 321$  pixels. Fig. 17 displays the visual comparison results for four images from 45 test images, where the green and blue outlines indicate manual segmentations and initialization results in Fig. 17(a), and the white outlines in (b)–

(f) represent the final segmentations with different models. The visual comparison results illustrate that the RLSF model has better segmentation performance than the state-of-art approaches. The segmentation accuracy (Jaccard index) and Hausdorff distance for the segmentation results obtained by using five algorithms to segment 45 Berkeley color images are displayed in Fig. 18. It demonstrated that the RLSF model achieves higher Jaccard index and lower hausdorff distance, and outperforms the other models. Both quantitative comparisons demonstrated that the RLSF model has a good performance for the nature images. Parameters were set to be  $\lambda_1 = \lambda_2 = 1$ ,  $\mu = 0.06$ ,  $\epsilon = 0.01$ ,  $r = 10$ . The local window considered in the local similarity factor was set to a square of  $7 \times 7$  pixel dimensions.

## 5. Discussion and conclusion

The spatial distance in the RLSF was included to balance the intensity differences between neighboring pixels and local mean intensity on two sides of active contour, aiming for convergence to similarity factor pixels as the number of iterations increase. This spatial information changes adaptively according to the distance from the neighbor pixels to the center of the local window and the intensity difference varies automatically within a neighborhood region, changing the local similarity values from pixel to pixel and from iteration to iteration. Fig. 19 displays an example of this process in an image corrupted by Gaussian noise, showing the segmented contour results and contents of the level set function  $\Phi$  values within a neighboring  $5 \times 5$  window at increasing number of iterations, from initialization in (a) to 1500 iterations in (d). According to the function values shown in Fig. 19, we can observe how those values evolve to positive values within the object and negative values for the background. The suppression extent of uncorrupted pixels within the local neighborhood becomes stronger because the local intensity difference depresses the influence of more noisy pixels. Moreover, when neighbor pixels are mostly corrupted by noise, the ability of balancing noise primarily depends on the local spatial distances. Hence, the local similarity factor balances the influence of the noisy pixels.

In this paper, we present a novel region-based active contour model via local similarity factor. The proposed algorithm shows promising results segmenting objects of different nature and characteristics in images of different nature at higher values of noise level, where other known methods seem to fail. This is achieved by incorporating a local spatial distance and intensity difference factors.

While our method seems to be more robust to higher noise levels and provides outlines of sufficient detail preservation, similarly to many traditional region-based active contour models, the RLSF model is sensitive to the active contour initialization. We plan to include further modifications and constraints to make it less sensitive to this initialization as well as improve its ability to handle more complex images in upcoming work.

## Acknowledgments

The authors would like to express their gratitude to the anonymous referees for their valuable comments. This work was supported by China Scholarship Council, 201406840031, the Six Talent Peaks Project in Jiangsu Province (2014-SWX-024), the Fundamental Research Funds for the Central Universities under Grant no. 30920140111004, the National Science Foundation of China under Grant no. 61473310.

## References

- [1] M. Kass, A. Witkin, D. Terzopoulos, Snakes: active contour models, *Int. J. Comput. Vis.* 1 (4) (1988) 321–331.
- [2] Ning Xua, Narendra Ahuja, Ravi Bansal, Object segmentation using graph cuts based active contours, *Comput. Vision. Image Underst.* 107 (3) (2007) 210–224.
- [3] V. Caselles, Illes Balears Univ, Spain Palma De Mallorca, R. Kimmel, G. Sapiro, Geodesic active contours, *Proc. IEEE Int. Conf. Comput. Vis.* (1995) 694–699.
- [4] V. Caselles, R. Kimmel, G. Sapiro, Geodesic active contours, *Int. J. Comput. Vis.* 22 (1) (1997) 61–79.
- [5] T. Chan, L. Vese, Active contour without edges, *IEEE Trans. image Process.* 10 (2) (2001) 266–277.
- [6] G.P. Zhu, Sh. Q. Zhang, Q.S.H. Zeng, Ch.H. Wang, Boundary-based image segmentation using binary level set method, *SPIE OE Lett.* 46 (5) (2007).
- [7] C.M. Li, C.Y. Xu, C.F. Gui, M.D. Fox, Level set evolution without re-initialization: a new variational formulation, in: *Proceedings of the IEEE Conference on Computer Vision and Pattern Recognition*, San Diego, 2005, pp.430–436.
- [8] N. Paragios, R. Deriche, Geodesic active contours and level sets for detection and tracking of moving objects, *IEEE Trans. Pattern Anal. Mach. Intell.* 22 (2000) 1–15.
- [9] N. Paragios, R. Deriche, Geodesic active regions and level set methods for supervised texture segmentation, *Int. J. Comput. Vis.* 46 (2002) 223–247.
- [10] R. Malladi, J.A. Sethian, B.C. Vemuri, Shape modeling with front propagation: a level set approach, *IEEE Trans. Pattern Anal. Mach. Intell.* 17 (1995) 158–175.
- [11] A. Vasilievskiy, K. Siddiqi, Flux-maximizing geometric flows, *IEEE Trans. Pattern Anal. Mach. Intell.* 24 (2002) 1565–1578.
- [12] J. Lie, M. Lysaker, X.C. Tai, A binary level set model and some application to Mumford–Shah image segmentation, *IEEE Trans. Image Process.* (2006) 1171–1181.
- [13] D. Mumford, J. Shah, Optimal approximation by piecewise smooth function and associated variational problems, *Commun. Pure Appl. Math.* 42 (1989) 577–685.
- [14] A. Tsai, A. Yezzi, A.S. Willsky, Curve evolution implementation of the Mumford–Shah functional for image segmentation, denoising, interpolation, and magnification, *IEEE Trans. Image Process.* 10 (2001) 1169–1186.
- [15] L.A. Vese, T.F. Chan, A multiphase level set framework for image segmentation using the Mumford–Shah model, *Int. J. Comput. Vis.* 50 (2002) 271–293.
- [16] R. Ronfard, Region-based strategies for active contour models, *Int. J. Comput. Vis.* 46 (2002) 223–247.
- [17] L. Chen, Y. Zhou, Y. Wang, J. Yang, GACV: geodesic-aided C–V method, *Pattern Recognit.* 39 (7) (2006) 1391–1395.
- [18] C.M. Li, C. Kao, J. Gore, Z. Ding, Implicit active contours driven by local binary fitting energy, in: *Proceedings of the IEEE Conference on Computer Vision and Pattern Recognition*, 2007, pp.1–7.
- [19] C. Li, C. Kao, J. Gore, Z. Ding, Minimization of region-scalable fitting energy for image segmentation, *IEEE Trans. Image Process.* 17 (2008) 1940–1949.
- [20] H. Liu, Y. Chen, W. Chen, Neighborhood aided implicit active contours, *IEEE Conf. Comput. Vision. Pattern Recognit.* 1 (2006) 841–848.
- [21] K.H. Zhang, H.H. Song, L. Zhang, Active contours driven by local image fitting energy, *Pattern Recognit.* 43 (4) (2010) 1199–1206.
- [22] Shawn Lankton, Allen Tannenbaum, Localizing region-based active contours, *IEEE Trans. Image Process.* 17 (11) (2008) 2029–2039.
- [23] L. Wang, Z. Yu, C. Pan, Medical image segmentation based on novel local order energy, in: *Proceedings of the Asian Conference on Computer Vision*, 2010, pp.148–159.
- [24] L. Wang, C. Pan, Robust level set image segmentation via a local corepoint-based K-means clustering, *Pattern Recognit.* 47 (5) (2014) 1917–1925.
- [25] Y. Han, W. Wang, X. Feng, A new fast multiphase image segmentation algorithm based on non-convex regularizer, *Pattern Recognit.* 45 (1) (2012) 363–372.
- [26] S. Liu, Y. Peng, A local region-based Chan–Vese model for image segmentation, *Pattern Recognit.* 45 (7) (2012) 2769–2779.
- [27] Q. Ge, L. Xiao, J. Zhang, Z. Wei, An improved region-based model with local statistical features for image segmentation, *Pattern Recognit.* 45 (4) (2012) 1578–1590.
- [28] Y. Wang, S. Xiang, C. Pan, L. Wang, G. Meng, Level set evolution with locally linear classification for image segmentation, *Pattern Recognit.* 46 (6) (2013) 1734–1746.
- [29] K. Zhang, L. Zhang, M. Lam, D. Zhang, A locally Statistical Active Contour Model for Image Segmentation with intensity inhomogeneity, arXiv:1305.7053, 2013.
- [30] L. Wang, C.M. Li, Q.S. Sun, D.S. Xia, C.Y. Kao, Active contours driven by local and global intensity fitting energy with application to brain MR segmentation, *Comput. Med. Imaging Graph.* 33 (7) (2009) 520–531.
- [31] S. Osher, J.A. Sethian, Fronts propagating with curvature-dependent speed: algorithms based on Hamilton–Jacobi formulations, *J. Comput. Phys.* 79 (1988) 12–49.
- [32] Z. Ji, Y. Xia, Q. Sun, G. Cao, Q. Chen, Active contours driven by local likelihood image fitting energy for image segmentation, *Inf. Sci.* 301 (2015) 285–304.
- [33] Mark Sussman, Peter Smereka, Stanley Osher, A level set approach for computing solutions to incompressible two-phase flow, *J. Comput. Phys.* 114 (1) (1994) 146–159.
- [34] M.J. Swain, D.H. Ballard, Color indexing, *Int. J. Comput. Vis.* 7 (1991) 11–32.
- [35] C. Tomasi, R. Manduchi, Bilateral filtering for Gray and Color Images, in: *Proceedings of the IEEE international conference on computer vision*, Bombay, 1998, pp.839–846.

**Sijie Niu** received B.S. and Master Degrees from the school of Computer science at Liaocheng University and Southwest University of Science and Technology in 2007 and 2012, respectively. He is currently a Ph.D. Candidate in the school of Computer Science and Engineering, Nanjing University of Science and Technology, China, and is a visiting student at Stanford University. His research interests include Pattern recognition, machine learning, image analysis, and bio-information processing.

**Qiang Chen** received B.Sc. degree in computer science and Ph.D. degree in Pattern Recognition and Intelligence System from Nanjing University of Science and Technology, China, in 2002 and 2007, respectively. Currently, he is an associate professor in the School of Computer Science and Technology at the Nanjing University of Science and Technology. His main research topics are image segmentation, object tracking, image denoising, and image restoration.